

Turbulent transport of impurities and their effect on energy confinement

I. Pusztai^{1,3}, A. Mollén¹, T. Fülöp¹, J. Candy²

¹ Department of Applied Physics, Chalmers University of Technology and Euratom-VR Association, Göteborg SE-41296, Sweden

² General Atomics, P.O. Box 85608, San Diego, CA 92186-5608, USA

³ Plasma Science and Fusion Center, Massachusetts Institute of Technology, Cambridge, MA 02139, USA

E-mail: pusztai@chalmers.se

Abstract. By presenting linear and nonlinear gyrokinetic studies, based on a balanced neutral beam injection deuterium discharge from the DIII-D tokamak, we demonstrate that impurities alter the scaling of the transport on the charge and mass of the main species, and even more importantly, they can dramatically change the energy transport even in relatively small quantities. A poloidally varying equilibrium electrostatic potential can lead to a strong reduction or sign change of the impurity peaking factor due to the combined effect of the in-out impurity density asymmetry and the $\mathbf{E} \times \mathbf{B}$ drift of impurities. We present an approximate expression for the impurity peaking factor and demonstrate that impurity peaking is not significantly affected by impurity self-collisions.

1. Introduction

Several models have been proposed to explain the favorable isotope mass scaling of the energy confinement in tokamaks [1, 2, 3, 4, 5], yet a commonly accepted and robust theoretical explanation of the isotope effect which is consistent with the other experimentally established parameter scalings [6, 7, 8, 9] is still lacking. When the turbulent energy transport is determined by the properties of the main ion species, dimensional considerations suggest that the charge and mass scaling of the heat diffusivities, χ , should follow the gyro-Bohm scaling, $\chi_{gB} \sim \rho_i^2 v_i / a \propto \sqrt{m_i} / Z_i^2$, where $v_i = (2T_i/m_i)^{1/2}$ is the ion thermal speed, a is the plasma minor radius, $\rho_i = v_i / \Omega_{ci}$ is the ion thermal Larmor radius, with the cyclotron frequency $\Omega_{ci} = Z_i e B / m_i$ of an ion of charge number Z_i and mass m_i , and B is the magnetic field strength. Studies of charge and mass effects on the turbulent energy transport in DIII-D tokamak plasmas show that the presence of impurities can contribute to deviations from a pure gyro-Bohm scaling [11]. In this paper we use the expression “pure gyro-Bohm” if differences in the turbulence between similar plasmas with different main species can be exactly transformed out by normalizing temporal and spatial scales to a/v_i and ρ_i , respectively.

In the first part of the paper we present *similarity studies*, that is, a series of gyrokinetic (GK) simulations with GYRO [10] where the local geometry and profile parameters – taken from a deuterium discharge studied in Ref. [11] – are kept fixed while the ion composition is artificially changed from case to case. First the effect of impurities (in particular, carbon or deuterium) on energy transport in hydrogen isotope and helium plasmas is studied. Then we investigate the role of the main species on impurity transport, and conclude that impurity transport does not follow the pure gyro-Bohm scaling (based on the properties of the main ion species) so closely as the energy transport.

One of the ways to reduce impurity accumulation in tokamak cores is to apply central radio frequency (RF) heating [12, 13, 14, 15]. RF-heating can generate poloidal impurity density asymmetries [16] and if the asymmetry is sufficiently strong, it can lead to a sign change in the impurity peaking factor [17, 18]. Recently it was shown that a sign change of the impurity peaking factor can happen at much weaker (that is, realistic) asymmetry strengths than were considered in Ref. [18] if the $\mathbf{E}_\theta \times \mathbf{B}_\phi$ drift of impurities in the poloidally varying equilibrium electrostatic field is taken into account [19]. In the second part of this paper, we extend the work of Ref. [19], by including parallel dynamics and finite Larmor radius (FLR) effects and modeling impurity self-collisions with the full linearized operator for impurity self-collisions to derive an improved approximate expression for the impurity peaking factor.

2. Charge and mass effects on turbulent transport

In this section we study how the charge and mass scalings of the energy transport are affected by the presence of impurities, through linear and nonlinear GK similarity studies with GYRO, based on local profile and magnetic geometry data from an L-mode phase of a weakly rotating DIII-D deuterium discharge (129135, 1250-1300 ms). For detailed information on the resolution of the simulations and on the studied discharge we refer the reader to Ref. [11]. The dominant impurity in the discharges studied in Ref. [11] was carbon, and the hydrogen and helium discharges had a significant deuterium fraction present; this motivates our choice of impurities in the simulations presented in this section. We neglect particle flows within the flux surface and to model different ion compositions we keep the electron density profile fixed and assume constant ion concentrations. For different main species with the same charge the results of local GK simulations – normalized to main ion species units – should exactly coincide when impurities and collisions are neglected and adiabatic electron response is assumed [11]. Thus we normalize growth rates, γ to c_{si}/a , where $c_{si} = (T_e/m_i)^{1/2}$, binormal wave numbers k_y to $1/\rho_{si} = \Omega_{ci}/c_{si}$, and fluxes to gyro-Bohm units $Q_{gBi} = n_e T_e c_{si} (\rho_{si}/a)^2$, $\Gamma_{gBi} = n_e c_{si} (\rho_{si}/a)^2 \propto m_i^{1/2}/Z_i^2$.

In Figs. 1 (a,b) the growth rate of linear modes at $k_y \rho_{si} = 0.3$ (at $r/a = 0.55$) is shown as a function of carbon concentration n_C/n_e . The local geometry and profile parameters, in the notation of Ref. [10], are: $q = 1.78$, $s = 0.75$, $\kappa = 1.34$, $\delta = 0.11$,

$a/L_n = 0.68$, $a/L_{Ti} = 1.89$, $a/L_{Te} = 2.69$, $T_i/T_e = 0.82$, $\nu_{ei} = 0.14 c_s/a$. The solid line corresponds to a deuterium plasma, the dashed is a hydrogen and the dotted is a helium plasma. We also show simulations for diluted deuterium plasma (long dashed lines), i.e., the deuterium concentration is decreased to the value that would correspond to the given carbon concentration (according to $n_i/n_e = 1 - Z_C n_C/n_e$), but the carbon has no response to fluctuations (the carbon density is set to zero in the simulation). Fig. 1 (a) shows the simulation results with adiabatic electrons. The decrease in the growth rates with increasing carbon concentration is practically linear. For lower carbon concentrations the slope of the γ curves is the same in main ion species units, independently of the mass or charge of the main species. For higher carbon concentrations a small difference between hydrogen isotopes and helium appears regarding the slopes, but the deuterium and hydrogen curves still overlap almost exactly, in spite of the difference between the m_C/m_i mass ratios. Noticeable deviations between growth rates in different hydrogen isotope plasmas appear only at higher wave numbers; noting that $1/\rho_{sC} \approx 2.45/\rho_{si}$.

Figure 1 (b) shows trapped electron (TE) mode growth rates in a collisionless drift-kinetic electron simulation. The TE modes are weakly destabilized as the impurity concentration is increased and this effect is somewhat stronger in hydrogenic plasmas. This destabilization is due to the increased weight of trapped-electrons in the Poisson equation due to the diluting effect of impurities (similarly, the stabilizing effect of impurities on ITG modes mentioned before is mostly due to the decreased weight of ions). But it has to be noted that these TE modes are strongly stabilized when electron-ion collisions are introduced in the simulation, and the stabilizing effect of increasing Z_{eff} appearing in the electron-ion collision frequency can be much stronger than the destabilizing effect observed in the collisionless case.

Finally, we compare the deuterium plasma simulations with the correct physics (solid lines) to the model where only the diluting effect of impurities is taken into account (long dashed lines). The presence of carbon contributes to a further stabilization of the ITG modes, and this contribution is comparable to the effect of the dilution of the main species. However, for the TE mode, the presence of carbon has almost negligible effect compared to that caused by the dilution of the main species.

Moving on to nonlinear simulations, the curves in Figs. 1 (c-f) represent the distribution of energy (or particle) fluxes over poloidal wave numbers; the $k_\theta \rho_{si}$ integral of the curves give the fluxes in gyro-Bohm units; the corresponding flux values are given in the plot legends. The nonlinear simulations include kinetic electron response and electron-ion collisions and they are based on the local parameters of the studied deuterium plasma at $r/a = 0.65$ ($q = 2.08$, $s = 1.1$, $\kappa = 1.36$, $\delta = 0.14$, $a/L_n = 0.79$, $a/L_{Ti} = 1.94$, $a/L_{Te} = 3.07$, $T_i/T_e = 0.91$, $\nu_{ei} = 0.23 c_s/a$).

First, we study the respective and combined effects of the carbon and deuterium impurities on energy transport. Figure 1 (c) shows the *total* ion energy flux in species units for a pure hydrogen plasma (solid curve), in hydrogen plasmas with carbon (dashed) and deuterium (dash-dotted) impurities, and with both carbon and deuterium

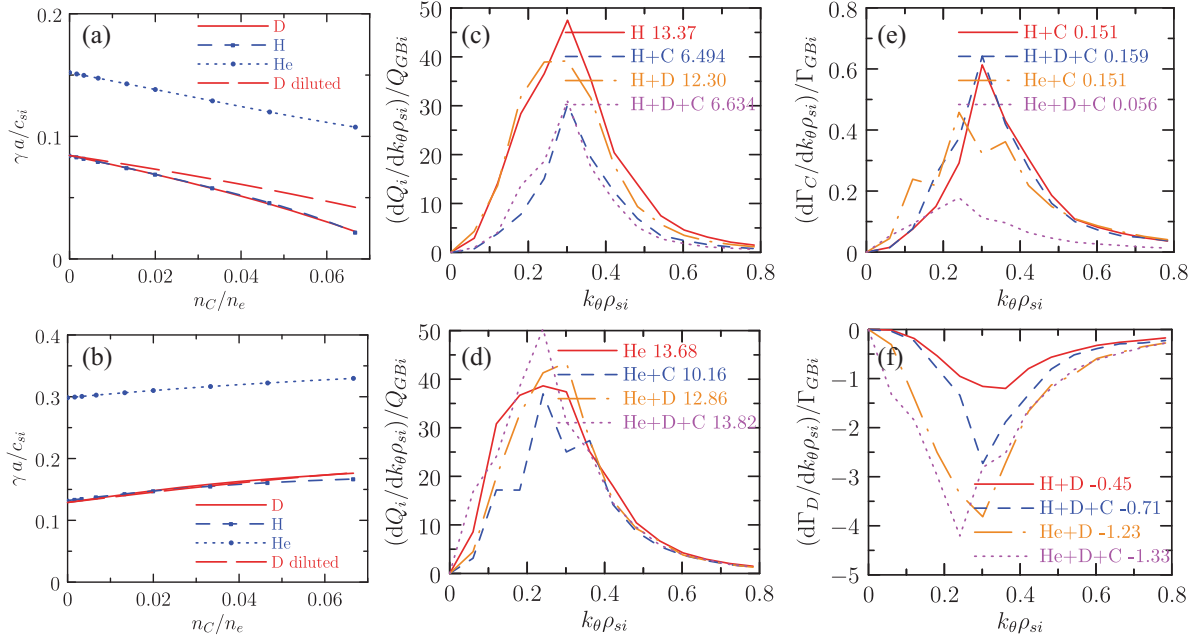


Figure 1. (a,b) Growth rates of the $k_y\rho_{si} = 0.3$ mode as a function of carbon concentration. Solid: main ion species is deuterium, dashed: hydrogen, dotted: helium, long dashed: diluted deuterium (no carbon, non-quasineutral). (c,d) Ion energy flux spectra [in D units] of pure plasmas (solid), with carbon (dashed), with deuterium (dash-dotted), and with carbon and deuterium impurities. (c): main ion hydrogen, (d): helium. (e) and (f): carbon and deuterium particle flux spectra.

impurities (dotted); $n_C/n_i = 0.04167$ corresponding to $Z_{\text{eff}} = 2$ in hydrogenic plasmas, and $n_D/n_i = 1/3$. The stabilizing effect of carbon on ITG modes, seen also in the linear simulations, appears as a strong reduction (by 51%) of the ion energy fluxes that acts at all wave numbers (we note that TE modes are stabilized by collisions). The presence of deuterium slightly reduces the transport at higher wave numbers (this feature is consistent with corresponding linear simulation results, not shown here). Interestingly, when there is carbon impurity in the plasma, the presence of a deuterium minority does not reduce the absolute value of the transport, only the spectrum gets shifted slightly towards lower wave numbers. The effect of these impurities is qualitatively the same on the electron energy flux, the difference is that the reduction in the electron energy transport is not as strong as in the ion energy transport (only 35%). Figure 1 (d) shows how the presence of D and C affects the energy transport in a helium plasma. The effect of a C impurity is considerably weaker in a helium plasma than in hydrogen isotope plasmas and it is concentrated to lower wave numbers. The fact that we kept n_C/n_i fixed in the simulations [shown in Figs. 1 (c) and (d)] instead of n_C/n_e is part of the reason why we find a weaker effect of carbon in the simulation with helium than with hydrogen main ions, since then carbon density is smaller in the helium plasma. However, even if we kept n_C/n_e fixed, looking at Fig. 1 (a) we expect to have a weaker impact of the carbon impurity on transport because the relative change in the linear

growth rates (compared to the pure plasma case) for given carbon concentration is smaller in a helium plasma than in hydrogen. While both carbon and deuterium act to reduce the energy transport in the helium plasma (compare the gyro-Bohm normalized fluxes in the legend of Fig. 1 (d)), interestingly, when both impurities are present the absolute value of the transport remains almost the same as in the pure plasma, however the shape of the energy flux spectra changes somewhat, being more peaked around its maximum.

In Figs. 1 (e,f) the carbon and deuterium particle fluxes are shown in impure hydrogen and helium plasmas, respectively (positive sign corresponding to an outward particle flux). In species units the magnitude of the carbon particle flux is the same in a hydrogen and a helium plasma when the ratio n_C/n_i is kept fixed; compare the solid and dash dotted curves in Fig. 1 (e). The shape of the carbon particle flux spectra are similar to the ion energy flux spectra in the hydrogen and helium plasmas [H+C and He+C curves in Figs. (c,d) compared to those in Fig. (e)], however, the magnitude of Q_i is smaller in the H+C than in the He+C plasma. It is also interesting to note, that in the hydrogen plasma the carbon particle flux remains almost unaffected when a deuterium minority is introduced; in contrast to the helium plasma, where the carbon flux drops dramatically (by 63%) in the presence of deuterium; a trend opposite to what was found for ion energy fluxes.

Figure 1 (f) shows that the deuterium particle fluxes in species units appear to be almost three times higher in a helium plasma than in a hydrogen plasma, even if the n_D/n_i values are held constant, so the number of deuterium particles is half as many in the helium plasma as in the hydrogen plasma. In spite of the fact that the linear growth rates and the energy transport are reduced when carbon impurity is present, the deuterium particle fluxes increase both in a H(+D) and a He(+D) plasma when carbon impurity is introduced.

3. Impurity peaking factor in the presence of poloidal asymmetries

In this section we calculate the zero flux density gradient (peaking factor) of trace impurities under the effect of a poloidally varying equilibrium electrostatic potential ϕ_E that can arise due to e.g. the presence of a species with strong temperature anisotropy [20]. Especially, in case of RF heating on the outboard side, the trapped population of the heated particle species increases in the vicinity of the resonance position [21, 16]. The peaking factor depends on the linear mode characteristics and on the form of ϕ_E . Here, we neglect effects caused by a radial electric field, such as toroidal rotation.

We assume $e\Delta\phi_E/T_j \ll 1$, where $\Delta\phi_E$ refers to the poloidal variation of ϕ_E , so that poloidal asymmetry effects on the main species can be neglected; this assumption is needed to justify the use of GYRO simulations to obtain the linear mode characteristics. However, we allow for $Ze\Delta\phi_E/T_z = \mathcal{O}(1)$.

3.1. Perturbed impurity distribution

We consider the particle transport driven by a single, representative, toroidal mode. The impurity peaking factor is calculated by requiring the linear impurity flux $\Gamma_z \equiv \Im \langle -k_y \hat{n}_z \phi^* / B \rangle = \Im \langle -k_y \int d^3v J_0(z_z) g_z \phi^* / B \rangle$ to vanish (steady state is assumed and impurity sources are neglected). Here $\langle \cdot \rangle$ denotes a flux surface average, \hat{n}_z is the perturbed impurity density, g_z the non-adiabatic part of the perturbed impurity distribution function, J_0 is the Bessel function of the first kind, $z_z = k_\perp v_\perp / \omega_{cz}$, $k_\perp = (1 + s^2 \vartheta^2)^{1/2} k_y$, and the rest of the notation is standard. The species indexes z , e and i refer to impurities, electrons and main ions.

The linearized GK equation is to be solved to obtain the non-adiabatic part of the impurity distribution function g_z ,

$$\left. \frac{v_\parallel}{qR} \frac{\partial g_z}{\partial \vartheta} \right|_{\mathcal{E}, \mu} - i(\omega - \omega_{Dz} - \omega_E) g_z - C[g_z] = -i \frac{Z e f_{z0}}{T_z} (\omega - \omega_{*z}^T) \phi J_0(z_z), \quad (1)$$

where ϑ is the extended poloidal angle, $\omega = \omega_r + i\gamma$ is the mode frequency, $f_{z0}(\psi, \mathcal{E}) = n_{z0}(\psi) [m_z / 2\pi T_z(\psi)]^{3/2} \exp[-\mathcal{E}/T_z(\psi)]$ is the equilibrium Maxwellian distribution. $\mu = m_z v_\perp^2 / (2B)$, $\mathcal{E} = m_z v^2 / 2 + Ze\phi_E$, $\omega_{*z}^T = \omega_{*z} [1 - L_{nz} Ze \partial_r (\phi_E e \phi_E / T_z - 3/2) L_{nz} / L_{Tz}]$ with $\omega_{*z} = -k_y T_z / Ze B L_{nz}$, $L_{nz} = -[\partial_r (\ln n_z)]^{-1}$ and $L_{Tz} = -[\partial_r (\ln T_z)]^{-1}$. Furthermore, $\omega_{Dz} = -2k_y / m_z (\mathcal{E} - Ze\phi_E - \mu B / 2) \mathcal{D}(\vartheta) / \omega_{cz} R$, where $\mathcal{D}(\vartheta) = \cos \vartheta + s \vartheta \sin \vartheta$. The $\mathbf{E} \times \mathbf{B}$ drift frequency in the equilibrium electrostatic field is $\omega_E = k_y [\partial_r \phi_E - s \vartheta \partial_\vartheta (\phi_E) / r] / B$. Our ordering $Ze\phi_E / T_z \sim \mathcal{O}(1)$ requires that ω_E / ω is formally $\sim 1/Z$ small; this requirement is mostly satisfied for experimentally relevant poloidal asymmetries. We consider ion scale modes, $z_i \lesssim 1$, and we allow the parallel streaming term of main ions to be comparable to the mode frequency. In the following we perform a perturbative solution of the impurity GK equation (1) in the small parameter $Z^{-1/2} \ll 1$. We assume that impurity self-collisions dominate over unlike-particle collisions, requiring $n_z Z^2 / n_e = \mathcal{O}(1)$, thus we model only impurity-impurity collisions with the full linearized collision operator $C_{zz}^{(l)}[\cdot]$.

Keeping in mind that ω_E / ω , ω_{Dz} / ω , ω_{*z}^T / ω , and $J_0(z_z) - 1 \approx -z_z^2 / 4$ are all $\sim 1/Z$ small, the lowest order equation $-i\omega g_0 - C_{zz}^{(l)}[g_0] = -i\omega Ze\phi f_{z0} / T_z$ for $g_z = g_0 + g_1 + g_2 + \dots$ is satisfied by $g_0 = Ze\phi f_{z0} / T_z$, since $C_{zz}^{(l)}[g_0 \propto f_{z0}]$ vanishes. To first order in $Z^{-1/2}$, we have $v_\parallel \partial_\vartheta (g_0) / (qR) - i\omega g_1 - C_{zz}^{(l)}[g_1] = 0$. Using $C_{zz}^{(l)}[g_1 \propto v_\parallel f_{z0}] = 0$, and $\partial_\vartheta (f_{z0})|_{\mathcal{E}} = 0$, we obtain $g_1 = -iZe f_{z0} v_\parallel \partial_\vartheta (\phi) / (T_z \omega q R)$. To next order, the GK equation reads

$$-i\omega g_2 - C_{zz}^{(l)}[g_2] = -i(\omega_{Dz} + \omega_E) g_0 - v_\parallel \partial_\vartheta (g_1) / (qR) + iZe\phi f_{z0} (\omega z_z^2 / 4 + \omega_{*z}^T) / T_z. \quad (2)$$

Using that $m_z v_\parallel \partial_\vartheta (v_\parallel)|_{\mathcal{E}, \mu} = -\mu \partial_\vartheta B - Ze \partial_\vartheta \phi_E$, the parallel compressibility term in the right hand side of Eq. (2), can be expressed as

$$-\frac{v_\parallel}{qR} \frac{\partial g_1}{\partial \vartheta} = i \frac{Ze f_{z0}}{\omega T_z q^2 R} \left\{ v_\parallel^2 \frac{\partial}{\partial \vartheta} \left(\frac{1}{R} \frac{\partial \phi}{\partial \vartheta} \right) - \frac{1}{R} \frac{\partial \phi}{\partial \vartheta} \left[\frac{v_\perp^2}{2} \frac{\partial \ln B}{\partial \vartheta} + \frac{Ze}{m_z} \frac{\partial \phi_E}{\partial \vartheta} \right] \right\}. \quad (3)$$

We decompose the magnetic drift frequency and the FLR parameter as $\omega_{Dz} = \omega_{Dx} + \omega_{D\parallel}$ and $z_z^2 = z_x^2 - z_{\parallel}^2$, where ω_{Dx} and z_x^2 are proportional to v^2 and $\omega_{D\parallel}$ and z_{\parallel}^2 are proportional to v_{\parallel}^2 . Also, we write $g_2 = \hat{g}_2 + \tilde{g}_2$, where \hat{g}_2 has contributions proportional to f_{z0} and $v^2 f_{z0}$, thus $C_{zz}^{(l)}[\hat{g}_2] = 0$. The collisionless, isotropic part of Eq. (2) is solved by

$$\hat{g}_2 = \frac{\omega_{Dx} + \omega_E}{\omega} g_0 - \frac{Ze\phi}{T_z} f_{z0} \frac{\omega z_x^2/4 + \omega_{*z}^T}{\omega} + \frac{Zef_{z0}}{\omega^2 T_z q^2 R^2} \frac{\partial \phi}{\partial \vartheta} \left[\frac{v^2}{2} \frac{\partial \ln B}{\partial \vartheta} + \frac{Ze}{m_z} \frac{\partial \phi_E}{\partial \vartheta} \right]. \quad (4)$$

Then \tilde{g}_2 should satisfy the remaining part of Eq. (2) which, upon division by $-i\omega$ reads

$$\tilde{g}_2 - \frac{i}{\omega} C_{zz}^{(l)}[\tilde{g}_2] = \frac{\omega_{D\parallel}}{\omega} g_0 + \frac{Ze\phi}{T_z} f_{z0} \frac{z_{\parallel}^2}{4} - \frac{Zev_{\parallel}^2 f_{z0}}{\omega^2 T_z q^2 R} \left\{ \frac{\partial}{\partial \vartheta} \left[\frac{1}{R} \frac{\partial \phi}{\partial \vartheta} \right] + \frac{1}{2R} \frac{\partial \phi}{\partial \vartheta} \frac{\partial \ln B}{\partial \vartheta} \right\}. \quad (5)$$

Equation 5 can be written as $\tilde{g}_2 - \frac{i}{\omega} C_{zz}^{(l)}[\tilde{g}_2] - X v_{\parallel}^2 f_{z0} = 0$, where X is independent of velocity. The solution can be written in the form $\tilde{g}_2 = \Xi(\mathbf{v}) f_{z0}$, where Ξ can incorporate any nontrivial velocity dependence. Taking the density moment of Eq. (5)

$$\int d^3v [\tilde{g}_2 - i C_{zz}^{(l)}[\tilde{g}_2]/\omega - X v_{\parallel}^2 f_{z0}] = 0. \quad (6)$$

Since $\int d^3v C_{zz}^{(l)}[\Xi(\mathbf{v}) f_{z0}] = \int d^3v \Xi(\mathbf{v}) C_{zz}^{(l)}[f_{z0}] = 0$, Eq. (6) can be reduced to $\int d^3v [\tilde{g}_2 - X v_{\parallel}^2 f_{z0}] = 0$.

Since we are only interested in the density moment of the perturbed distribution function needed to evaluate the impurity peaking factor, instead of solving the complicated collisional equation (5) unnecessarily, we derive a substitute function \tilde{g}_{2s} that has the same density moment as \tilde{g}_2 ; we choose $\tilde{g}_{2s} = X v^2 f_{z0}/3$.

We introduce a substitute function for g_z , denoted by g_s , with the property $\int d^3v J_0(z_z) g_s = \int d^3v J_0(z_z) g_z + \mathcal{O}(Z^{-2})$; we define it as $g_s = g_0 + \hat{g}_2 + \tilde{g}_{2s}$, that reads

$$\frac{g_s T_z}{Ze f_{z0}} = \phi \left[1 + \frac{4\omega_{Dx}/3 + \omega_E - \omega_{*z}^T}{\omega} - \frac{z_x^2}{6} \right] - \frac{v_z^2}{3(\omega q R)^2} \left[x_z^2 \frac{\partial^2 \phi}{\partial \vartheta^2} - \frac{3}{2} \frac{\partial \phi}{\partial \vartheta} \frac{\partial}{\partial \vartheta} \left(\frac{Ze\phi_E}{T_z} \right) \right], \quad (7)$$

where $x_z = v/v_z$, with $v_z = (2T_z/m_z)^{1/2}$. It is important to emphasize, that g_s is *not* an approximate solution to Eq. (1), but merely a function that has the same density moment as the solution. Taking other velocity moments of this function would give erroneous results, and g_s cannot be used to proceed with the perturbative solution.

3.2. Zero flux impurity density gradient

To calculate the impurity peaking factor we assume a simple sinusoidal poloidal asymmetry of the form $Ze\phi_E/T_z = -\kappa \cos(\theta - \delta)$ where κ is the asymmetry strength and δ determines the poloidal position of the impurity accumulation. When evaluating the density moment of Eq. (7), we keep the $\mathcal{O}(Z^{-1})$ correction from $J_0(z_z)$ where it multiplies g_0 . Also, we neglect $\mathcal{O}(\epsilon)$ corrections when solving for a/L_{nz}^0 , the value of

a/L_{nz} where $\langle \Gamma_z \rangle = 0$, to find

$$\frac{a}{L_{nz}^0} = 2 \frac{a}{R_0} \langle \mathcal{D} \rangle_\phi + \frac{a}{r} s \kappa \langle \theta \sin(\theta - \delta) \rangle_\phi - \frac{2av_i}{(qR_0)^2 k_y \rho_i} \frac{Zm_i}{m_z} \frac{\omega_r}{\omega_r^2 + \gamma^2} \left\langle \left| \frac{\partial \phi}{\partial \theta} \right|^2 / |\phi|^2 \right\rangle_\phi, \quad (8)$$

where $\rho_i = v_i m_i / e B_0$, and $\langle \dots \rangle_\phi = \langle \dots \mathcal{N} |\phi|^2 \rangle / \langle \mathcal{N} |\phi|^2 \rangle$, with $\mathcal{N} = \exp[\kappa \cos(\theta - \delta)]$. The FLR terms do not appear in a/L_{nz}^0 , since their imaginary part is zero. The first and second terms of Eq. (8) represents the contributions from ω_D and ω_E , respectively. Since the last term of Eq. (8) contains only non-negative quantities, except ω_r , impurity parallel dynamics acts to increase(decrease) the impurity peaking if ω_r is negative(positive). Note, that we use the sign convention of GYRO; ω_r is negative for modes propagating in the ion diamagnetic direction. The impurity parallel compressibility term introduces a dependence on mode frequency, and also on the charge to mass ratio, consistently with Ref. [22].

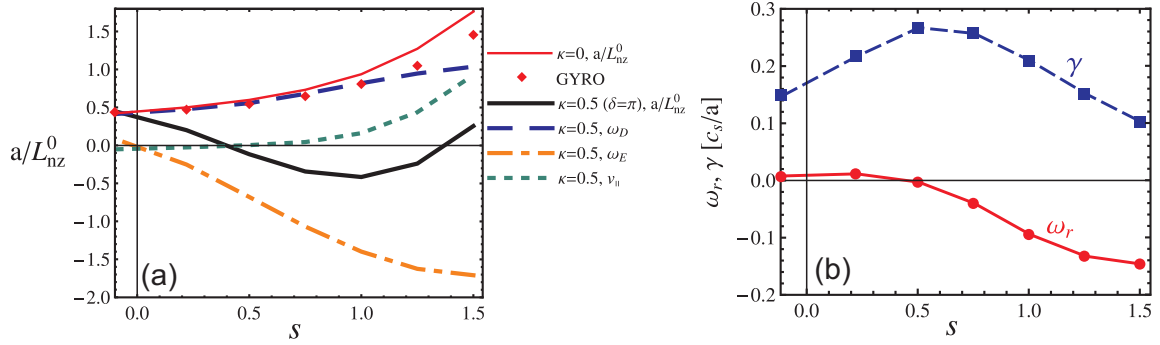


Figure 2. (a) Shear dependence of the impurity peaking factor. Thin solid line represents the poloidally symmetric case; the corresponding GYRO results are shown with red diamonds. Thick solid line represents an in-out asymmetry, $\kappa = 0.5$. The contributions from the different terms in Eq. (8) are also plotted; dashed line: magnetic drifts, dash-dotted: $\mathbf{E} \times \mathbf{B}$ drifts, dotted line: parallel compressibility. (b) Shear dependence of ω_r and γ from GYRO.

The shear dependence of the peaking factor of a fully ionized Nickel impurity calculated from Eq. (8) is shown in Figure 2(a). The local profile and geometry parameters assuming a circular model Grad-Shafranov equilibrium are: $r/a = 0.3$, $R_0/a = 3$, $k_\theta \rho_s = 0.3$, $q = 1.7$, $a/L_{ne} = 1.5$, $T_i/T_e = 0.85$, $a/L_{Te} = 2$ and $a/L_{Ti} = 2.5$, and collisions are switched off in the simulations to avoid discrepancies due to the different collision operators in this paper and in GYRO. The poloidally symmetric case is shown with thin solid line and shows a relatively good agreement with the exact values obtained from GYRO simulations represented by the diamond markers; the differences towards higher magnetic shear appear as a result of an overestimation of the parallel compressibility term due to the approximations done in the derivation of Eq. (8). A scenario with in-out impurity asymmetry for the asymmetry strength $\kappa = 0.5$ is also plotted with thick solid line, together with the contributions from the different terms

in Eq. (8). Around $s = 0$ the contribution from ω_E (dash-dotted line) vanishes, and in this specific case the parallel compressibility term (dotted line) is also small due to the small value of ω_r ; the peaking factor is dominated by ω_D (dashed line). If $|\omega_r|/\gamma \ll 1$, that happens for lower shear in the case studied here [see Fig. 2 (b)], the frequency dependent part of the third term in Eq. (8) is small, thus parallel compressibility effects do not play an important role; see the dashed curve in Fig. 2 (a).

As the magnetic shear increases the ω_E term starts to reduce the peaking factor, since $\langle \theta \sin(\theta - \pi) \rangle_\phi$ is negative for moderately ballooning eigenfunctions. In Eq. (8) the shear dependent part of \mathcal{D} , and the ω_E term can be combined as $(as/R_0)\langle \theta \sin \theta \rangle_\phi (2 \pm \kappa/\epsilon)$, where $\epsilon = r/R_0$, and the plus(minus) sign applies for out-in(in-out) impurity asymmetry. Thus, if $\phi(\theta)$ and ω are only weakly dependent on shear, increasing shear is expected to reduce the impurity peaking in the in-out asymmetric case when $2 < \kappa/\epsilon$ [for our simulation parameters $\kappa/\epsilon = 5$]. From Eqs. (10) and (12) in Ref. [19] one can estimate the ratio of the asymmetry strength and the inverse aspect ratio; assuming $T_e \approx T_i \approx T_z$, and taking the limits $\alpha_T \gg 1$ and $\epsilon \ll 1$ so that $\epsilon\alpha_T$ is also small we obtain $\kappa/\epsilon \approx \alpha_T Z X_m / (1 + Z_{\text{eff}})$, where α_T is the minority temperature anisotropy, and X_m is the minority fraction.

4. Conclusions

In the present paper we first study how impurity transport is affected by the charge and mass of the main ion species and the ion composition, and what impact the impurities have on energy transport, then we consider the effect of a poloidally varying equilibrium potential on impurity peaking.

Linear gyrokinetic analysis shows that for increasing impurity concentration the growth rates change in a linear fashion; in main ion species units the change in the growth rates when increasing impurity concentration to a given value – i.e. the slope of the $\gamma a/c_{si}(n_C/n_e)$ curves – is almost independent of the charge and mass of the main species. In the studied case, based on local profile and geometry data in a deuterium discharge from DIII-D, for ITG modes carbon impurity has a strongly stabilizing, – for TE modes (when neglecting collisions) a weak destabilizing – effect. For TE modes the effect is almost purely due to plasma dilution, for ITG modes the presence of the impurity itself has a comparable effect to the dilution that still dominates. The strong stabilizing effect of carbon in hydrogenic plasmas appears in nonlinear simulations as a strong reduction of energy transport, the relative change in the energy fluxes being even higher than that of the linear growth rates. The effect of impurities on energy transport is smaller in a helium plasma, due to the higher species units growth rates and the lower main ion concentration. The presence of deuterium mainly just changes the shape of the energy flux spectrum, although slightly reduces the transport in a hydrogen plasma. In general the presence of impurities, even in relatively small quantities, can cause significant deviations from a pure gyro-Bohm mass and charge scaling of energy fluxes. (Again, by “pure gyro-Bohm scaling” we refer to the situation when differences

in the turbulence between similar plasmas with different ion composition can be exactly transformed out by normalizing temporal and spatial scales to a/v_i and ρ_i , respectively. We do not mean that the transport is not gyro-Bohm in the general sense.)

We conclude that, while the apparent deviations from a pure gyro-Bohm scaling, – due to charge, electron-to-ion mass ratio or collisional effects, and importantly due to the presence of impurities, – can mostly be explained and understood from a linear analysis of the underlying microinstabilities, impurity transport do not follow these naive expectations. In particular, if we would normalize the impurity fluxes to ion energy fluxes we would get significantly different values in plasmas with different main ion species. Thus we might expect that the steady state impurity profiles would also vary in these plasmas (especially when impurity sources and neoclassical impurity transport are accounted for), causing further deviations from a pure gyro-Bohm scaling.

A poloidally varying electrostatic field, appearing due to e.g. a poloidally asymmetrically distributed RF heated particle species, even if being too weak to modify the dynamics of the main species, can essentially change impurity transport compared to a poloidally symmetric situation. We show that the combined effect of the arising poloidally asymmetric impurity distribution and the $\mathbf{E}_\theta \times \mathbf{B}_\phi$ drift of impurities can lead to a reduction or even a sign change in the impurity peaking factor. The effect becomes important at high impurity charge, when the magnetic and diamagnetic drifts (proportional to $1/Z$) become as small as the $\mathbf{E}_\theta \times \mathbf{B}_\phi$ drift in the poloidally varying equilibrium potential. We demonstrate that to lowest order in $1/Z$ finite Larmor radius effects and impurity collisions do not affect impurity peaking driven by ion scale microinstabilities as long as the impurity collisions are dominated by self-collisions and the impurity collision frequency is not much larger than the mode frequency. We present and analyze a simple analytical expression for the impurity peaking factor including contributions from the $\mathbf{E}_\theta \times \mathbf{B}_\phi$ drift and parallel compressibility, and depending on the linear mode characteristics. We find that to get sign change in the impurity peaking factor, a necessary criterion is that the ratio of the asymmetry strength κ and the inverse aspect ratio ϵ is larger than two.

Acknowledgments

The authors gratefully acknowledge discussions with P. J. Catto, P. Helander, S. Moradi and Ye. O. Kazakov. This work was funded by the European Communities under Association Contract between EURATOM and *Vetenskapsrådet*, and by the U.S. DOE under Contract Nos. DE-FG03-95ER54309 and DE-FG02-07ER54917 as part of the FACETS SciDAC project and used the resources of the NCCS at ORNL under Contract No. DEAC05-00OR22725.

References

- [1] J. Q. Dong, W. Horton, and W. Dorland, *Phys. Plasmas* **1**, 3635 (1994).

- [2] G. Bateman, A. Kritz, V. Parail, J. Cordey, and the JET Team, *Phys. Plasmas* **6**, 4607 (1999).
- [3] M. Tokar, D. Kalupin, and B. Unterberg, *Phys. Rev. Lett.* **92**, 215001 (2004).
- [4] R. Waltz, *Phys. Rev. Lett.* **93**, 239501 (2004).
- [5] D. Ernst, B. Coppi, S. Scott, M. Porkolab, and T. Group, *Phys. Rev. Lett.* **81**, 2454 (1998).
- [6] M. Bessenrodt-Weberpals *et al*, *Nucl. Fusion* **33**, 1205 (1993).
- [7] R. J. Hawryluk, *Rev. Mod. Phys.* **70**, 537 (1998).
- [8] J. Jacquinot and the JET team, *Plasma Phys. Control. Fusion* **41** (1999).
- [9] S. Scott *et al*, *Phys. Plasmas* **2**, 2299 (1995).
- [10] J. Candy and E. Belli, General Atomics Technical Report No. GA-A26818 (2010).
- [11] I. Pusztai, J. Candy, and P. Gohil, *Phys. Plasmas* **18**, 122501 (2011).
- [12] M. Valisa *et al*, *Nucl. Fusion* **51**, 033002 (2011).
- [13] R. Dux *et al*, and ASDEX Upgrade Team, *Plasma Phys. Control. Fusion* **45**, 1815 (2003).
- [14] M. E. Puiatti *et al*, *Phys. Plasmas* **13**, 042501 (2006).
- [15] R. Neu *et al*, *Nucl. Fusion* **45**, 209 (2005).
- [16] Ye.O. Kazakov, I. Pusztai, T. Fülöp, and T. Johnson, *Plasma Phys. Control. Fusion* **54**, 105010 (2012).
- [17] T. Fülöp and S. Moradi, *Phys. Plasmas* **18**, 030703 (2011).
- [18] S. Moradi, T. Fülöp, A. Mollén, and I. Pusztai, *Plasma Phys. Control. Fusion* **53**, 115008 (2011).
- [19] A. Mollén, I. Pusztai, T. Fülöp, Ye.O. Kazakov, and S. Moradi, *Phys. Plasmas* **19**, 052307 (2012).
- [20] M.L. Reinke *et al*, *Plasma Phys. Control. Fusion*, **54** 045004 (2012).
- [21] L.C. Ingesson *et al*, *Plasma Phys. Control. Fusion* **42**, 161 (2000).
- [22] C. Angioni and A. G. Peeters, *Phys. Rev. Lett.* **96**, 095003 (2006).